arXiv:1612.04231v2 [nucl-ex] 3 Mar 2017

Low-energy enhancement and fluctuations of γ-ray strength functions in ^{56,57}Fe: test of the Brink-Axel hypothesis

A. C. Larsen[1], M. Guttormsen[1], N. Blasi[2], A. Bracco[2,3], F. Camera[2,3], L. Crespo Campo[1], T. K. Eriksen[1,4], A. Görgen[1], T. W. Hagen[1], V. W. Ingeberg[1], B. V. Kheswa[1], S. Leoni[2,3], J. E. Midtbø[1], B. Million[2], H. T. Nyhus[1], T. Renstrøm[1], S. J. Rose[1], I. E. Ruud[1], S. Siem[1], T. G. Tornyi[1,4], G. M. Tveten[1], A. V. Voinov[5], M. Wiedeking[6], and F. Zeiser[1]

E-mail: a.c.larsen@fys.uio.no

[1] Department of Physics, University of Oslo, N-0316 Oslo, Norway

[2] INFN, Sezione di Milano, Milano, Italy

[3] Dipartimento di Fisica, University of Milano, Milano, Italy

[4] Department of Nuclear Physics, Australian National University, Canberra, Australia

[5] Department of Physics and Astronomy, Ohio University, Athens, Ohio 45701, USA

[6] iThemba LABS, P.O. Box 722, 7129 Somerset West, South Africa

January 2017

Abstract. Nuclear level densities and γ-ray strength functions of ^{56,57}Fe have been extracted from proton-γ coincidences. A low-energy enhancement in the γ-ray strength functions up to a factor of 30 over common theoretical E1 models is confirmed. Angular distributions of the low-energy enhancement in ^{57}Fe indicate its dipole nature, in agreement with findings for ^{56}Fe. The high statistics and the excellent energy resolution of the large-volume $LaBr_3$(Ce) detectors allowed for a thorough analysis of γ strength as function of excitation energy. Taking into account the presence of strong Porter-Thomas fluctuations, there is no indication of any significant excitation-energy dependence in the γ-ray strength function, in support of the generalized Brink-Axel hypothesis.

PACS numbers: 21.10.Ma, 21.10.-k, 27.40.+z, 25.20.Lj

Keywords: Level density, γ-strength function, angular distributions, Brink hypothesis, iron

Submitted to: *J. Phys. G: Nucl. Phys.*

1. Introduction

One of the long-standing experimental and theoretical challenges within nuclear physics is the determination of the nucleus' available quantum levels and the decay properties of these levels in the excitation-energy region between the ground state and up to the particle threshold(s). In this intermediate excitation-energy region, often called the *quasicontinuum*, the *nuclear level density* (NLD) and the average, reduced γ-decay probability, i.e. the *γ-strength function* (γSF), shed light on the dynamic behavior of the nucleus. Apart from providing information on basic nuclear properties, these quantities are also indispensable input for calculations of, e.g., neutron-capture cross sections. These cross sections are of great importance for applications such as the astrophysical heavy-element nucleosynthesis [1, 2] and modeling of next-generation nuclear power plants [3, 4].

Amongst a handful of experimental techniques, the Oslo method [5] has been established as one of the promising approaches to obtain experimental information on the NLD and γSF. The advantage of the Oslo method compared to other techniques is that both these quantities can be extracted from one and the same experiment, utilizing typically a charged-particle reaction to record particle-γ coincidences, in which the structural shape of the NLD and the γSF can be determined. By measuring the energy of the outgoing charged particle, the initial excitation energy of the residual nucleus is determined. The γ rays de-exciting this initial excitation energy are recorded in coincidence, thus obtaining γ spectra as function of initial excitation-energy.

In 2004, an unexpected enhancement of the γSF for low transition energies ($E_\gamma \lesssim 3$ MeV) was discovered in the iron isotopes ^{56,57}Fe [6]. This feature was not predicted by any theoretically derived γSFs; in fact, the γSF data showed an enhancement of more than a factor of 10 compared to typical models for the E1 strength [6]. In the following years this enhancement, also called *upbend*, was found in many medium-mass nuclei, including $^{43-45}$Sc [7, 8], ^{60}Ni [9], ^{73,74}Ge [10], and Mo isotopes [11, 12, 13]. To date, the heaviest nuclei where the upbend has been seen are ^{138,139}La [14] and ^{151,153}Sm [15]. The upbend was experimentally shown to be of dipole nature in ^{56}Fe [16]. Moreover, it has been demonstrated [17] that such a low-energy enhancement in the γSF could significantly increase radiative neutron-capture rates of relevance for the r-process – if found to be present in very neutron-rich nuclei.

In 2012, the upbend was independently confirmed in ^{95}Mo [12] using a different technique. This triggered theoretical investigations of the origin of this phenomenon. Within the thermal-continuum quasiparticle random-phase approximation (TCQRPA), the upbend was explained as due to $E1$ transitions caused by thermal single-quasiparticle excitations in the continuum [18], with its strength depending on the nuclear temperature. On the other hand, shell-model calculations [19, 20] show a strong increase in $B(M1)$ strength for low-energy $M1$ transitions. At present, ^{60}Ni is the only case where experimental data favor a magnetic character of the upbend [9]. More experimental information is needed in order to determine whether the upbend is

dominantly of magnetic or electric character, or a mixture of both.

In this work, we present NLDs and γSFs of ^{56,57}Fe extracted from (p,p′γ) coincidences, to be compared with data from other reactions using heavier projectiles, inducing higher initial spins. We analyze systematic errors in the normalization procedure and compare our results to available data in the literature. For the first time, we present angular distributions of the upbend in ^{57}Fe, as well as γSFs as function of excitation energy to investigate the so-called *generalized Brink-Axel hypothesis* for ^{56,57}Fe. This hypothesis has up to now only been validated for the heavy nucleus ^{238}Np [21].

This article is organized as follows. In section 2, we give experimental details and the main steps of the Oslo-method analysis. In section 3, the NLDs and γSFs are shown and the normalization uncertainties are discussed. Further, in section 4 angular distributions are presented for ^{57}Fe, while section 5 deals with γSFs as function of excitation energy and implications for the generalized Brink-Axel hypothesis. Finally, a summary and outlook are given in section 6.

2. Experimental details and data analysis

The experiments were performed at the Oslo Cyclotron Laboratory (OCL). A 16-MeV proton beam with intensity of ≈ 0.5 nA impinged on self-supporting targets of 99.9% enriched ^{56}Fe and 92.4% enriched ^{57}Fe. Both targets had mass thickness of ≈ 2 mg/cm^2. Accumulating times were ≈ 85h and ≈ 92h for ^{56,57}Fe, respectively.

The charged ejectiles were measured with the Silicon Ring particle-detector system (SiRi) [22] and the γ rays with the CACTUS array [23]. The SiRi system consists of eight $\Delta E - E$ telescopes. Each telescope is composed of a 130-μm thick front detector segmented into eight strips (angular resolution of $\Delta\theta \simeq 2^\circ$), and a 1550-$\mu$m thick back detector. In total, SiRi has 64 individual detectors and a solid-angle coverage of ≈ 6%. For these experiments, SiRi was placed in forward angles with respect to the beam direction, covering $40 - 54^\circ$. From the measured energy of the ejectiles and the reaction kinematics, the excitation energy of the residual nucleus is deduced.

In this experiment, the CACTUS array contained 22 collimated 5 *in.* × 5 *in.* NaI(Tl) detectors and six collimated 3.5 *in.* × 8 *in.* $LaBr_3$(Ce) detectors from the Milan HECTOR$^+$ array [24, 25]. The NaI detectors were placed on the CACTUS frame with six different angles θ with respect to the beam direction (37.4, 63.4, 79.3, 100.7, 116.6, and 142.6 degrees), while the $LaBr_3$ crystals covered four angles (63.4, 79.3, 100.7, and 116.6 degrees). The γ-energy thresholds were ≈ 400 keV and ≈ 800 keV for the NaI and $LaBr_3$ detectors, respectively. Particle-γ coincidences were recorded event-by-event, with the overlap of the ΔE and E detectors of SiRi as mastergate for the analog electronics. To obtain reasonable statistical error bars, i.e. ≈ 50% or better on the extracted NLD and γSF, about 40,000 coincidences are needed. In total, after background subtraction of random coincidences (about 10% of the prompt time peak), about 65 million coincidences were obtained for the NaI detectors and about 12 million

coincidences for the $LaBr_3$ detectors with the ^{56}Fe target. Correspondingly, for ^{57}Fe, about 15 million and 2.1 million coincidences were recorded for the NaI and $LaBr_3$ detectors, respectively. The time resolution of the SiRi-NaI detectors was 14.4(5) ns and for the SiRi-$LaBr_3$ detectors 6.3(3) ns.

In figure 1, the proton spectrum of SiRi in coincidence with γ rays from the present experiment is compared to the α spectrum from the previous experiment reported in Ref. [6]. The significant improvement in energy resolution is clear; the proton spectra have a full width at half maximum (FWHM) of ≈ 90 keV compared to the α spectra where FWHM ≈ 500 keV. The main reason for this improvement is the segmentation of the ΔE detectors in SiRi compared to the old setup with a non-segmented ΔE detector. The segmentation allows for a much more precise determination of the scattering angle and thus the recoil energy. Also, using a proton beam instead of a ^{3}He beam gives a smaller recoil energy to the residual nucleus. For more details, we refer to [22].

The proton-γ coincidence matrices for the NaI and $LaBr_3$ detectors are displayed in figure 2. The superior energy resolution for the $LaBr_3$ spectra relative to the NaI ones is evident, as well as diagonals for which the excitation energy E equals the γ energy E_γ corresponding to decay to the ground state. Other diagonals are also clearly visible, for example the direct decay to the first-excited 2^+ state in ^{56}Fe.

It is also very interesting to note the "triangles" in the ^{57}Fe matrix where the γ intensity suddenly drops, see for example at $E_\gamma \approx E \approx 8.5$ MeV in figure 2c,d. One would naively think that the γ intensity would be significantly reduced as soon as the

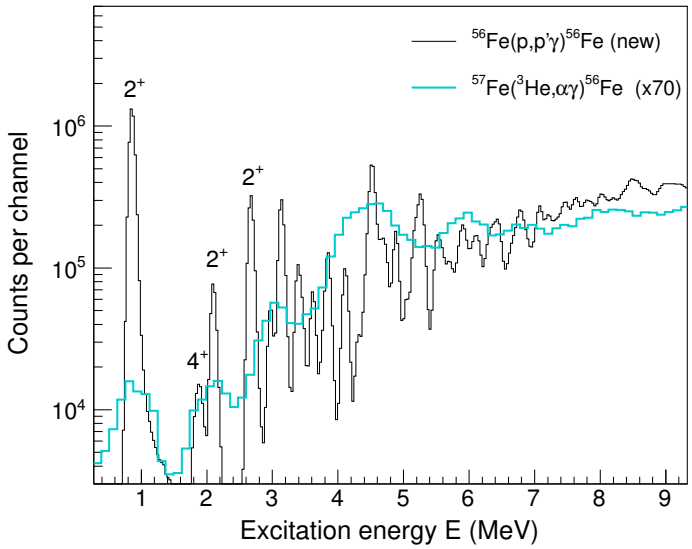

Figure 1. (Color online) Proton spectra (black histogram, this work) and α spectra [6] (thick cyan line, scaled with a factor of 70) in coincidence with γ rays measured with the CACTUS NaI detectors for ^{56}Fe. Energy bins are 31 keV/channel for protons and 123 keV/channel for αs. The first excited levels are marked with their spin/parity.

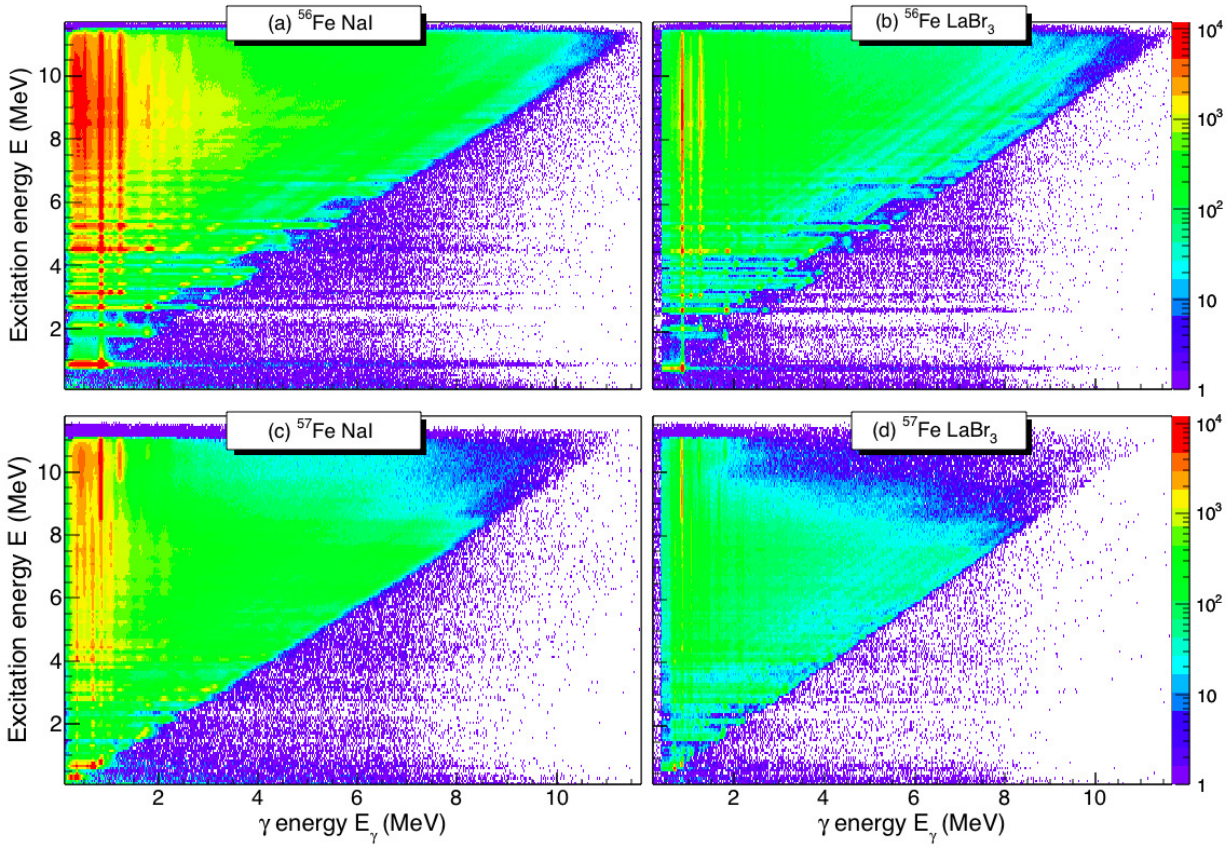

Figure 2. (Color online) γ-ray energy versus excitation energy before unfolding for (a) ^{56}Fe, NaI detectors; (b) ^{56}Fe, $LaBr_3$ detectors; (c) ^{57}Fe, NaI detectors; (d) ^{57}Fe, $LaBr_3$ detectors. Energy bins are 14 keV/channel.

neutron separation energy S_n is reached; however, this is well above $S_n = 7.646$ MeV. This feature is explained by considering the average spin $\langle J \rangle$ populated at high excitation energies. From γ transitions in coincindence with protons, we identify the decay from the 6^+ level at $E = 3.39$ MeV in ^{56}Fe as well as other levels with spins 2, 3, 4, 5 [16]. Levels with these spins will be hindered in decaying through s-wave neutron emission to the 0^+ ground state in ^{56}Fe. This hindrance is studied in detail for ^{95}Mo and applied in a novel technique to determine spins in [26].

In order to obtain the correct γ-energy distribution for each excitation-energy bin, the signals from the NaI and $LaBr_3$ detectors must be corrected for the detector response. We applied the unfolding technique described in [27], which is an iterative procedure using a strong smoothing of the Compton part of the spectrum. In order to construct response functions for the NaI and $LaBr_3$ detectors, we used in-beam measured transitions from ^{56}Fe, ^{28}Si, ^{13}C, and ^{16}O [28].

Moreover, we made use of a subtraction technique [29] to extract the distribution of primary γ rays, i.e. the first γ rays emitted in the decay cascades, for each excitation-

energy bin. This distribution contains information on the NLD and the γSF as deduced from Fermi's Golden Rule [30, 31]:

$$\lambda = \frac{2\pi}{\hbar} |\langle f|H'|i\rangle|^2 \rho_f, \tag{1}$$

where λ is the decay rate between initial state i and final state f, H' is the transition operator and ρ_f is the density of final states. Similarly, the distribution of primary γ rays as function of E depends on the level density at $E_f = E - E_\gamma$ and the γ-transmission coefficient $\mathcal{T}$ for the γ transition with energy E_γ. The γ-transmission coefficient is directly proportional to the γSF. Our ansatz is [5]:

$$P(E_\gamma, E) \propto \rho(E_f)\mathcal{T}(E_\gamma), \tag{2}$$

where $P(E_\gamma, E)$ is the matrix of primary γ rays, representing relative intensities or branching ratios for a given transition energy E_γ at a given initial excitation energy E.

The primary γ-ray matrices $P(E_\gamma, E)$ for ^{56,57}Fe are shown in figure 3. They are normalized for each excitation-energy bin so that $\sum_{E_\gamma} P(E_\gamma, E) = 1$. This means that the probability for γ decay from a given bin is 1, and that the intensity of a given γ-ray energy reflects the branching ratio for that particular transition energy.

These matrices are used as input for the extraction of the NLD and γSF for the four data sets. The expression in equation 2 is valid for statistical decay, i.e. where the decay is independent of the formation of the compound state [34]. This is fulfilled at rather high excitation energies where the initial NLD is high, typically above $\approx 2\Delta$ where the pair-gap parameter $\Delta \approx 12A^{-1/2}$ [34]. Note that $\mathcal{T}$ is a function only of E_γ and not E or E_f, in accordance with the generalized Brink-Axel hypothesis [32, 33]. This will be discussed in detail in section 5.

The functional form of the NLD and γSF is determined through a least-χ^2 fit to the $P(E_\gamma, E)$ matrices as described in [5]. The 3D landscapes as shown in figure 3 are used in the fit. The sum of all primary transitions for each E bin is normalized to unity. As the $P(E_\gamma, E)$ matrices contain many more data points ("pixels") than the free parameters (the vector elements of $\rho(E_f)$ and $\mathcal{T}(E_\gamma)$), the solution is uniquely determined and the fit routine converges fast, typically within 10-20 iterations.

Some considerations need to be made before extracting the NLD and γSF from the data. First, a low-energy limit for the excitation energy is applied to avoid the discrete region at low E, for which the condition of a compound-nucleus decay is highly questionable. Further, an upper limit $E_{\max}$ must be given, which typically corresponds to S_n, as neutrons are not measured or discriminated in the present experimental setup. Finally, a low-energy limit on the γ energy, $E_{\gamma,\mathrm{low}}$, is determined to exclude eventual higher-generation transitions not properly subtracted in the primary-distribution extraction, as discussed in detail in [35]. The chosen energy limits for the extraction procedure are: $E_{\gamma,\mathrm{low}} = 2.1$ MeV, $E_{\min} = 6.6$ MeV, and $E_{\max} = 11.3$ MeV for ^{56}Fe; correspondingly, $E_{\gamma,\mathrm{low}} = 1.4$ MeV, $E_{\min} = 5.0$ MeV, and $E_{\max} = 8.2$ MeV for ^{57}Fe. The neutron separation energies S_n are 11.197 MeV and 7.646 MeV for ^{56,57}Fe, respectively. The reason why we are able to put $E_{\max}$ higher than S_n in the

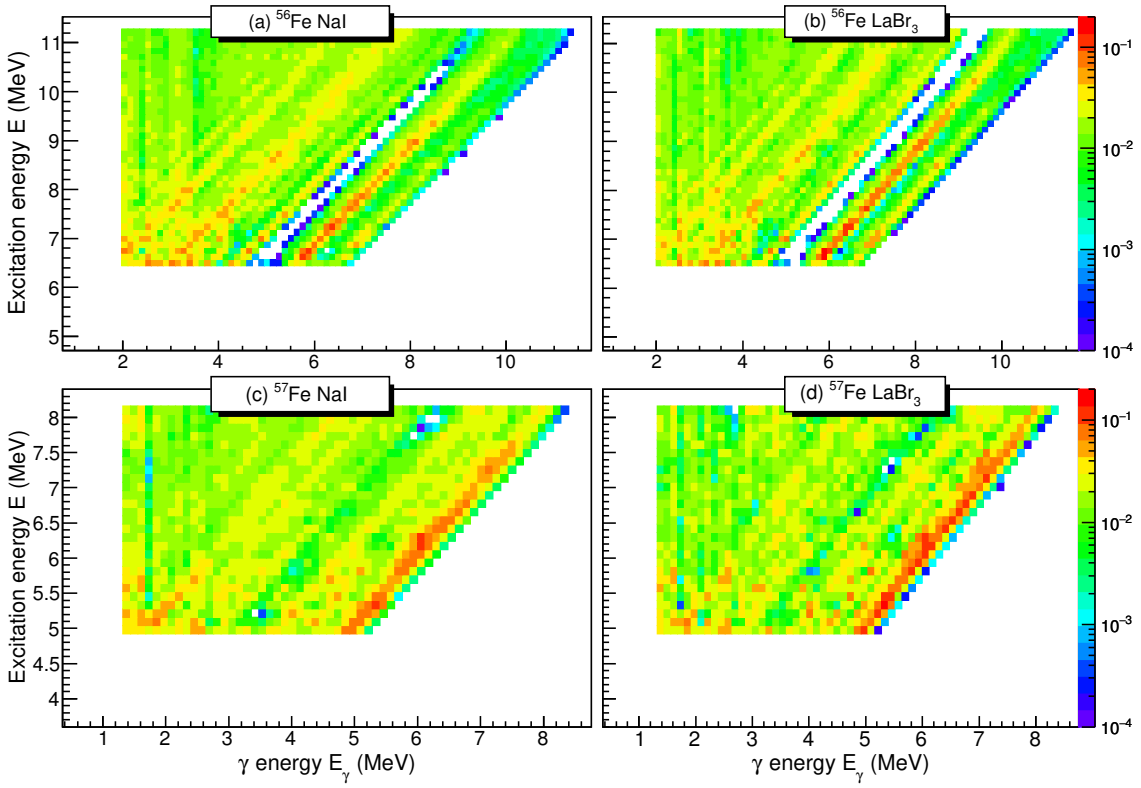

Figure 3. (Color online) Distribution of primary γ rays energy versus excitation energy for (a) ^{56}Fe, NaI detectors; (b) ^{56}Fe, $LaBr_3$ detectors; (c) ^{57}Fe, NaI detectors; (d) ^{57}Fe, $LaBr_3$ detectors. Energy bins are 124 keV/channel for ^{56}Fe and 120 keV/channel for ^{57}Fe. Note the different energy scales for the lower and upper panels.

case of ^{57}Fe, is that the first-excited state in ^{56}Fe is at 847 keV, allowing in principle for $E_{\rm max} = (7.65 + 0.85)$ MeV $= 8.5$ MeV as we are requiring proton-γ coincidences. Similarly, for ^{57}Fe, the upper limit is ≈ 100 keV above S_n.

To test the quality of the fit, which is based on all primary spectra included in the extraction procedure, we take the obtained $\rho(E_f)$ and $\mathcal{T}(E_\gamma)$ functions and use them to generate primary γ spectra to be compared with the input spectra bin by bin. This is shown in figure 4. Error bars in the primary spectra reflect statistical uncertainties, and systematic uncertainties stemming from the unfolding procedure and the extraction of the primary γ rays [5].

As can be seen from figures 4–7, the overall agreement between the data and the calculated primary spectra is very good. It should be noted that Porter-Thomas fluctuations [36] of the decay strengths are not taken into account. These fluctuations are expected to be large when the final level density ρ_f is low. This is clearly visible *e.g.* in the decay to the first-excited level in ^{56}Fe, see figure 4a and the peak at $E_\gamma \approx 6.5$ MeV, where data points are several standard deviations off the calculated $\rho \times \mathcal{T}$. Here, there is only one final level and the relative decay strength is seen to fluctuate strongly

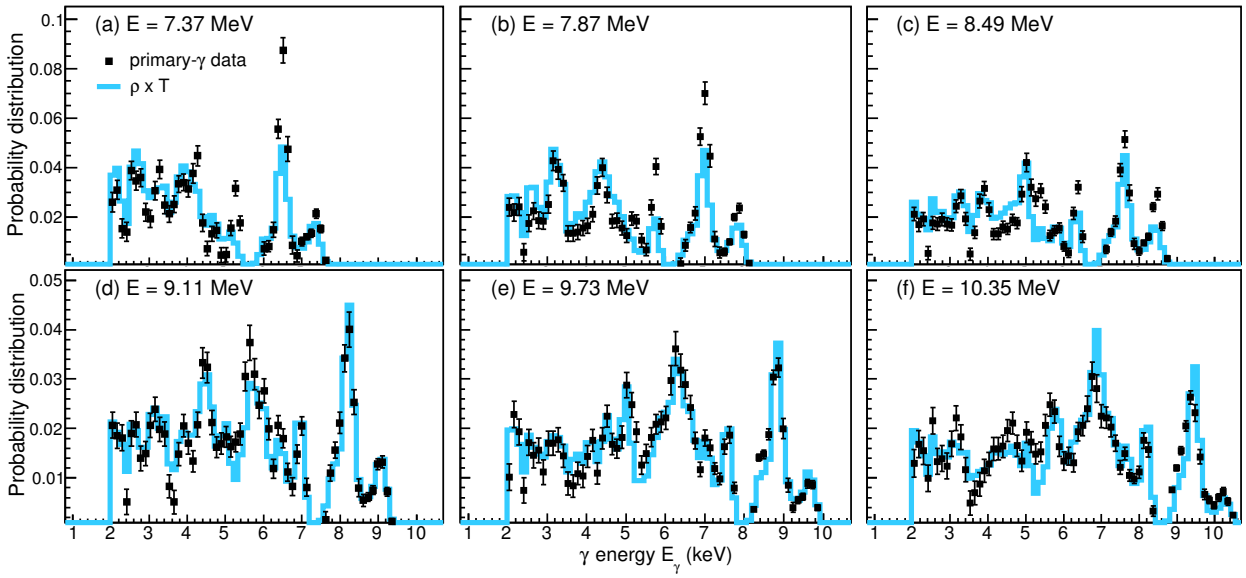

Figure 4. (Color online) Comparison of experimental primary γ spectra for ^{56}Fe (black points, NaI detectors) with the calculated ones (blue histogram) from the extracted ρ and $\mathcal{T}$ functions for a set of initial excitation-energy bins as indicated in the panels. Energy bins are 124 keV/channel.

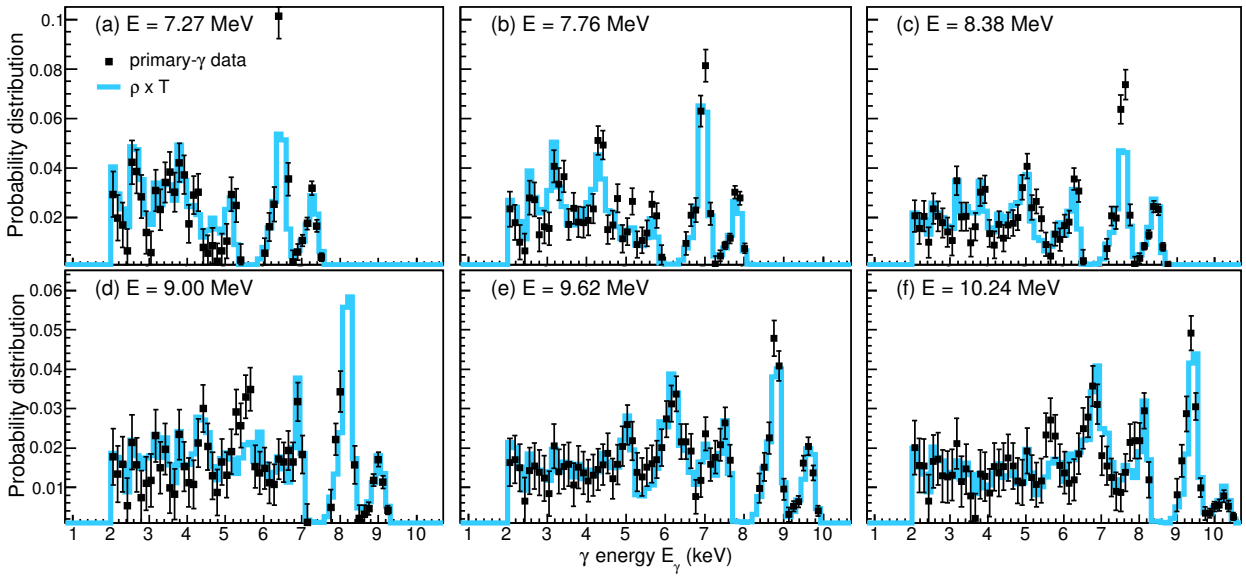

Figure 5. (Color online) Same as figure 4 for ^{56}Fe, using data from the $LaBr_3$ detectors.

for different initial excitation energies.

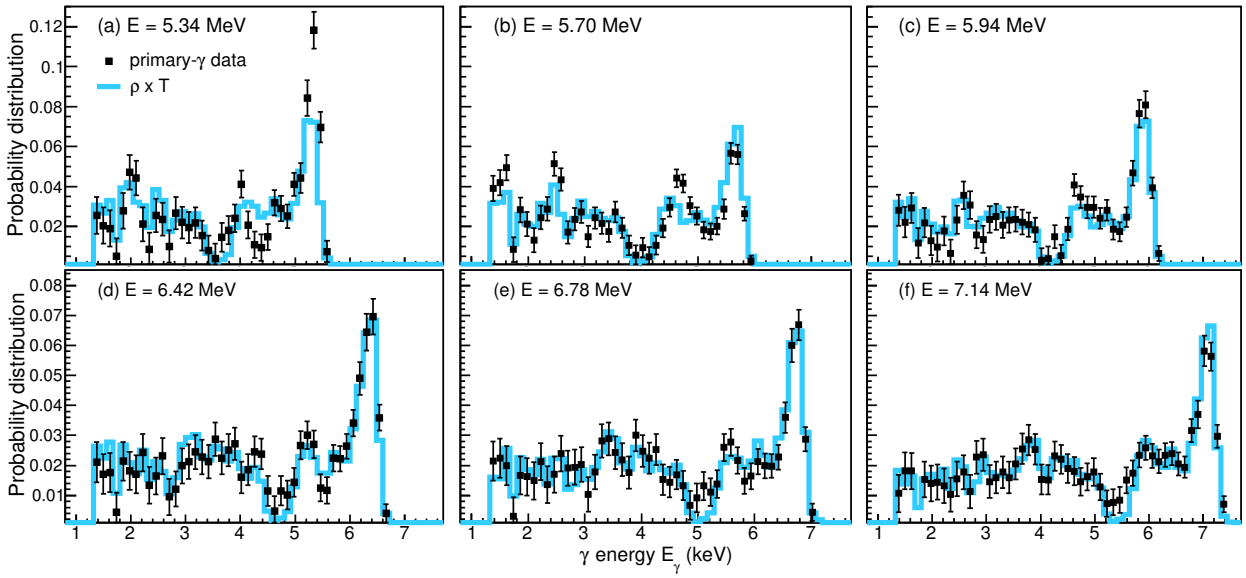

Figure 6. (Color online) Same as figure 4 for ^{57}Fe measured with NaI detectors. Energy bins are 120 keV/channel.

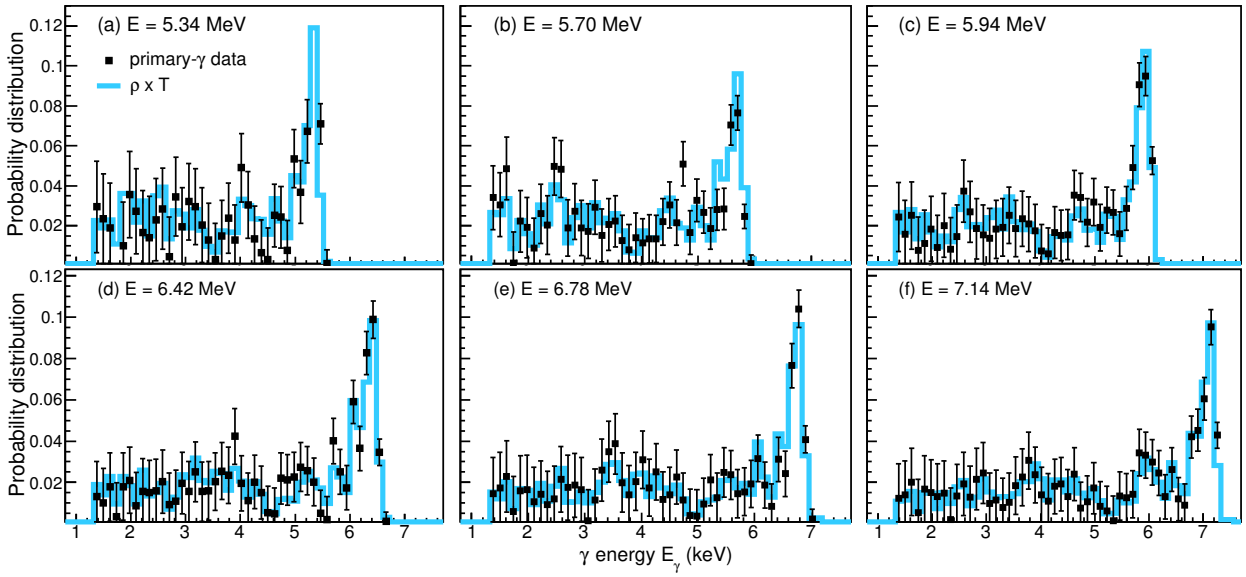

Figure 7. (Color online) Same as figure 4 for ^{57}Fe using data from the $LaBr_3$ detectors.

3. Level density and γ strength

3.1. Normalization

As only the functional form of the NLD and γSF can be deduced from the primary γ spectra, the slope and absolute normalization must be determined from auxiliary data.

It is shown in [5] that any solution $\tilde{\rho_f}$ and $\tilde{\mathcal{T}}$ will give an equally good χ^2 fit to the primary-γ data through the transformations

$$\rho(E - E_\gamma) = \mathcal{A} \exp[\alpha(E - E_\gamma)]\, \tilde{\rho}(E - E_\gamma), \tag{3}$$

$$\mathcal{T}(E_\gamma) \quad = \mathcal{B} \exp(\alpha E_\gamma) \tilde{\mathcal{T}}(E_\gamma), \tag{4}$$

where the parameters $\mathcal{A}$, $\mathcal{B}$, are the absolute normalization of the NLD and the γ-transmission coefficient, respectively, and α is the common slope parameter.

For the NLD, the parameters $\mathcal{A}$ and α are found by fitting our data to known levels from the literature [37] at low excitation energy and to neutron-resonance spacing data from [38] at S_n. The discrete levels are binned with the same bin width as our experimental data. For ^{56}Fe, there is no information from neutron-resonance experiments as ^{55}Fe is unstable. For this case, we have estimated the NLD at S_n from systematics in the following way:

(i) To estimate the lower-limit NLD, we calculate the total level density from the s-wave neutron resonance spacing D_0 for Fe isotopes where this value is available from [38] according to the expression

$$\rho(S_n) = \frac{2\sigma^2}{D_0} \cdot \frac{1}{(J_t+1)\exp\left[-(J_t+1)^2/2\sigma^2\right] + J_t \exp\left[-J_t^2/2\sigma^2\right]}, \tag{5}$$

assuming equally many positive- and negative-parity states. Here, J_t is the ground-state spin of the target nucleus in the neutron-resonance experiment and σ is the spin cutoff parameter. We make use of the phenomenological spin cutoff parameter suggested in [40]:

$$\sigma^2(E) = 0.391 A^{0.675} (E - 0.5Pa')^{0.312}. \tag{6}$$

Here, A is the mass number and Pa' is the deuteron pairing energy as defined in [40]. This approach gives a low value for the spin cutoff parameter and thus a low limit for the level density. Further, we calculate $\rho(S_n)$ from the global systematics [40] directly. By taking the χ^2 fit of the semi-experimental $\rho(S_n)$ with the values from systematics in the same fashion as done for ^{89}Y in [39], one obtains an estimate for the ^{56}Fe $\rho_{\rm low}(S_n)$. All parameters are given in table A1. This normalization is referred to as *norm-1* in the following.

(ii) To estimate the upper-limit NLD, we apply the same procedure as in (i) but with the spin cutoff parameter given by the rigid-body moment of inertia approach as parameterized in [41]:

$$\sigma^2(E) = 0.0146 A^{5/3} \frac{1 + \sqrt{1 + 4a(E - E_1)}}{2a}. \tag{7}$$

Here, a is the level-density parameter and E_1 is the excitation-energy backshift determined from global systematics of [41]. All parameters are given in table A2. We refer to this normalization as *norm-2*.

For ^{57}Fe, we use the D_0 value given in [38] and estimate $\rho(S_n)$ using equation 5, again with spin cutoff parameters both from [40] and [41]. Consistent with the approach

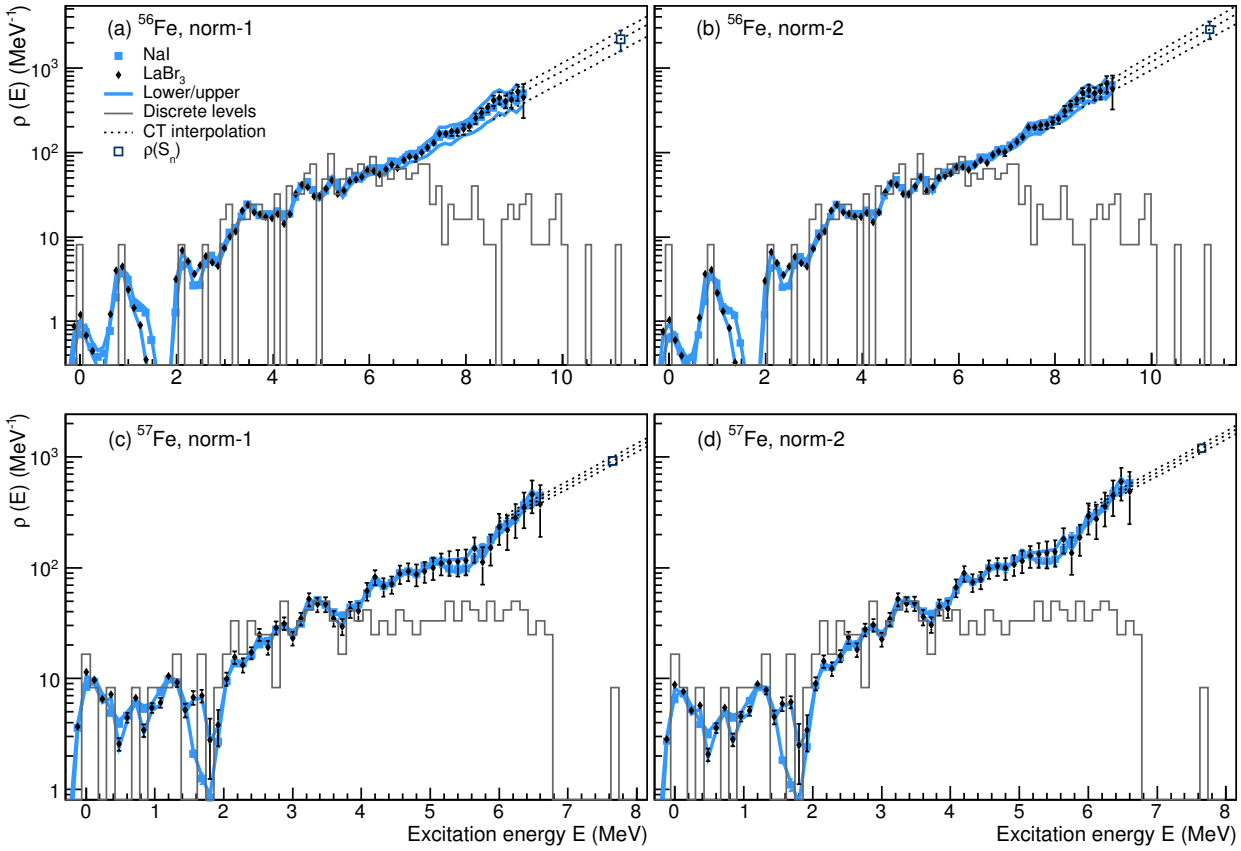

Figure 8. (Color online) Normalized level densities for (a) ^{56}Fe, norm-1, (b) ^{56}Fe, norm-2, (c) ^{57}Fe, norm-1, and (d) ^{57}Fe, norm-2.

for ^{56}Fe, the lower limit is obtained with the spin cutoff parameter in equation 6, and the upper limit with the one in equation 7, also including the uncertainties in D_0. All parameters are listed in table A1 and A2 in Appendix A.

As our data reach up to $E_{\max} - E_{\gamma,\mathrm{low}}$, we must interpolate between the estimated $\rho(S_n)$ and our upper data points. This is done using the constant-temperature formula of Ericson [42, 43]:

$$\rho_{CT}(E) = \frac{1}{T} \exp \frac{E - E_0}{T}. \tag{8}$$

The applied parameters T and E_0 are given in table A3 for the various normalization options, giving the best fit to our data in the regions $E = 8.2-9.2$ MeV and $E = 6.2-6.6$ MeV for ^{56,57}Fe, respectively. The normalized level densities are shown in figure 8.

With the normalized NLDs at hand, and assuming equal parity [44], we normalize the γ-ray transmission coefficient $\mathcal{T}$ to the average, total radiative width $\langle\Gamma_{\gamma 0}\rangle$ taken from [38] (see table A1) according to [44]

$$\langle\Gamma_{\gamma 0}(S_n, J_t \pm 1/2, \pi_t)\rangle = \frac{\mathcal{B}}{4\pi\rho(S_n, J_t \pm 1/2, \pi_t)} \int_{E_\gamma=0}^{S_n} \mathrm{d}E_\gamma \mathcal{T}(E_\gamma)$$

$$\times \rho(S_n - E_\gamma) \sum_{J=-1}^{1} g(S_n - E_\gamma, J_t \pm 1/2 + J), \quad (9)$$

where J_t and π_t are the spin and parity of the target nucleus in the (n,γ) reaction and $\rho(S_n - E_\gamma)$ is the experimental NLD. Note that the experimental transmission coefficient in principle includes all types of electromagnetic transitions: $\mathcal{T}_{E1} + \mathcal{T}_{M1} + \mathcal{T}_{E2} + ...$; however, dipole transitions are found to be dominant for decay in the quasicontinuum (e.g., [16, 45]). The sum in equation 9 runs over all final states with spins $J_t \pm 1/2 + J$, where $J = -1, 0, 1$ from considering the spins reached after one primary dipole transition with energy E_γ (see also equation 3.1 in [45]). Note that the factor $1/\rho(S_n, J_t \pm 1/2, \pi_t)$ equals the neutron resonance spacing D_0. From the normalized transmission coefficient, the γSF is determined by

$$f(E_\gamma) = \frac{\mathcal{T}(E_\gamma)}{2\pi E_\gamma^3}. \quad (10)$$

Again, ^{56}Fe lacks neutron resonance data and we have therefore estimated $\langle\Gamma_{\gamma 0}\rangle$ from a linear fit to the values of the other Fe isotopes taken from [38], see table A1. The normalized γSFs for the different normalization options for the level densities are shown in figure 9. The error band includes uncertainties in D_0, spin cutoff parameters, and $\langle\Gamma_{\gamma 0}\rangle$. We see that the γSFs have a distinct U-like shape, independent on the choice of normalization. There is a characteristic increase in strength at low transition energies, which is very similar in shape and magnitude to recent predictions from large-scale shell-model calculations [20].

At the highest γ-ray energies, we observe a drop in strength, which could be due to the reaction populating spins at high excitation energies that on average are higher than the (close-to) ground-state spin(s), and/or a small overlap with the wave functions for the initial and final levels. In particular, for ^{56}Fe, only 1^- and 1^+ levels contribute to the dipole strength to the ground state. For lower transition energies, a broad range of levels is available as the final level density is much higher. One should therefore note that the upper data points ($E_\gamma > 9.5$ and 7.2 MeV for ^{56,57}Fe, respectively) do not represent a general, averaged γSF in the quasicontinuum. The rather peculiar behavior of these data points indicate a possible (strong) dependence on the initial and final level(s), as well as significant Porter-Thomas fluctuations. This will be further investigated and discussed in section 5.

3.2. Comparison with other data

There exist data on the NLDs of ^{56,57}Fe from previous experiments at the OCL [6], using the ^{3}He-induced reactions ^{57}Fe(^{3}He,$\alpha\gamma$)^{56}Fe and ^{57}Fe(^{3}He,^{3}He$'\gamma$)^{57}Fe. Moreover, level densities have also been inferred from particle-evaporation spectra of the reactions ^{55}Mn(d,n)^{56}Fe [46], ^{59}Co(p,α)^{56}Fe [47], ^{58}Fe(^{3}He,α)^{57}Fe [48], and ^{60}Ni(n,α)^{57}Fe [49]. Reactions involving heavier projectiles and/or ejectiles, as well as detection angles in backward direction where the compound-reaction mechanism is dominant, populate

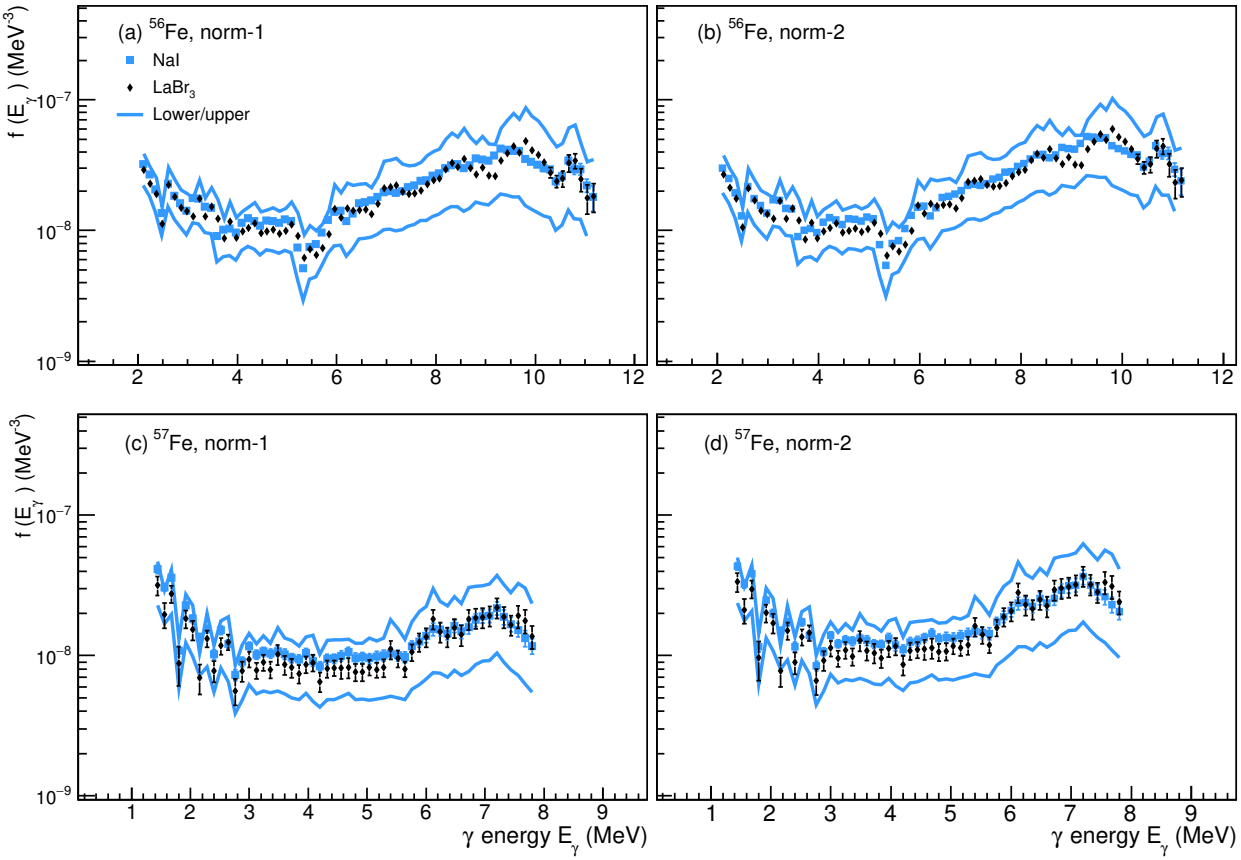

Figure 9. (Color online) Normalized γSFs for (a) ^{56}Fe, norm-1, (b) ^{56}Fe, norm-2, (c) ^{57}Fe, norm-1, and (d) ^{57}Fe, norm-2.

higher initial spins than for the (p, p') reaction in forward angles. This would help nailing down eventual reaction dependencies on the final results.

Figure 10 shows the comparison of the present data and previous results on the NLDs. We find that the overall agreement is very good, although there are some differences betweeen the data sets. For ^{56}Fe, we see that the particle-evaporation data give a higher NLD between $E \approx 5 - 7.5$ MeV, which is interpreted as due to the higher spins reached in these experiments compared to the proton inelastic scattering. The absolute normalization of our data is rather uncertain due to the lack of neutron-resonance data as discussed before; however, there is a significant boost in the number of levels at $E \approx 6$ MeV for all data sets relative to the known, discrete levels. For ^{57}Fe, a similar increase is taking place at $E \approx 4$ MeV. This could be caused by two factors: a quenching of pair correlations due to breaking of nucleon Cooper pairs, and sufficient energy to cross the $f_{7/2}$ shell gap with more than one particle (neutron or proton) into the $p_{3/2}, f_{5/2}, p_{1/2}$ orbitals.

We note that there is a significant deviation between the data of [48] and [49] above S_n for ^{57}Fe. It would be highly desirable to perform new experiments in this

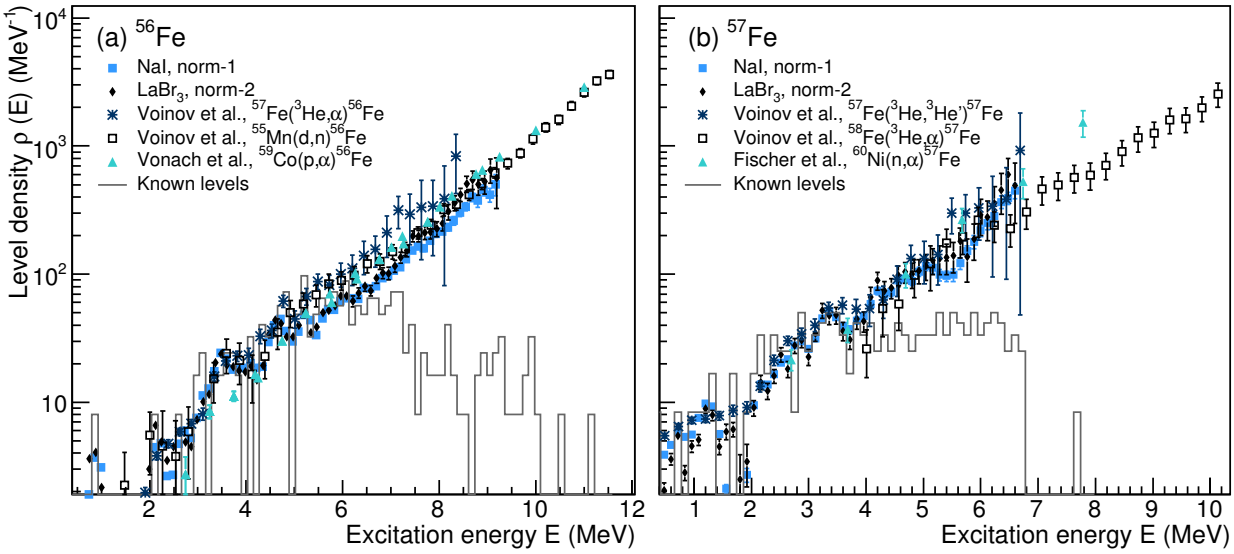

Figure 10. (Color online) Comparison of NLDs from different reactions for (a) ^{56}Fe and (b) ^{57}Fe. Previous data taken from [6, 46, 47, 48, 49].

energy region to clarify whether this is due to different spins populated, the particle transmission coefficients used in the analyses or issues with their absolute normalization to the discrete levels.

For the γSF, there are to our knowledge no photonuclear data available for ^{56,57}Fe. We have therefore compared our data to photoneutron (γ, n) cross sections of ^{55}Mn and ^{59}Co [50], and also an evaluation of the ^{56}Fe(γ, n) cross section [51]. The photoneutron cross section $\sigma_{\gamma n}$ maps out the shape of the Giant Dipole Resonance (GDR) [52], and is converted to γ strength by the relation [53]

$$f(E_\gamma) = \frac{1}{3\pi^2\hbar^2c^2}\frac{\sigma_{(\gamma,n)}(E_\gamma)}{E_\gamma}. \tag{11}$$

Moreover, data from threshold (γ, n) neutron-time-of-flight experiments on ^{57}Fe [54, 55, 56] provide an estimate for the $E1$ and $M1$ strength function at $E_\gamma \approx 7.7$ MeV; the sum of these are also compared to our data. The result is shown in figure 11, where we show only our normalizations for norm-1 and norm-2 for clarity. In general, we observe a very good agreement with the previous ^{3}He-induced data below S_n. We note that for ^{56}Fe, the slope of the γSF of [6] is somewhat steeper, leading to an overall lower strength for $E_\gamma < 4$ MeV and a higher strength above $E_\gamma \approx 7$ MeV. This is likely due to a different (steeper) NLD normalization as seen in figure 10a. For ^{57}Fe, a significant difference is only seen for E_γ above ≈ 6 MeV, where the ^{3}He-induced data undershoot the present results. The reason for this discrepancy is not clear; it could be related partly to different normalizations of the NLD, and/or strong transitions to the ground band for the (p, p') reaction that are less pronounced for the ^{3}He inelastic scattering.

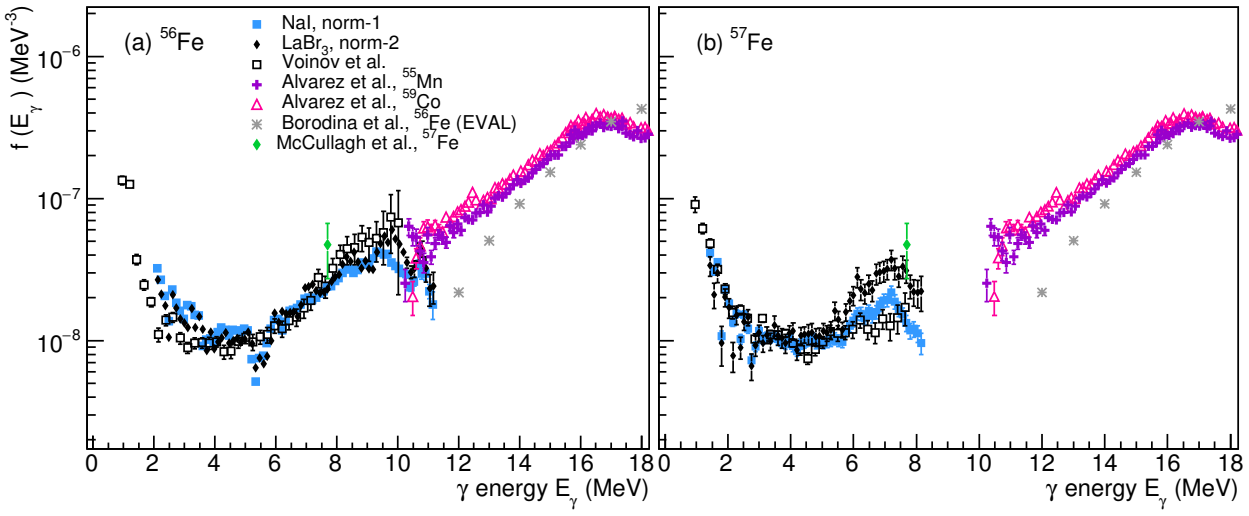

Figure 11. (Color online) Comparison of γSFs from different reactions for (a) ^{56}Fe and (b) ^{57}Fe. Photonuclear data are taken from [50], and the evaluated ^{56}Fe(γ, n) cross section from [51]. Also the ^{57}Fe $E1 + M1$ strength at $E_\gamma \approx 7.7$ MeV from resonant (γ, n) neutron time-of-flight measurements are shown [54, 55, 56]. For ^{56}Fe, the present work provides the γSF for $2.1 \leq E_\gamma \leq 11.3$ MeV, while data from [6] cover $1.0 \leq E_\gamma \leq 10.3$ MeV. Correspondingly, for ^{57}Fe, the present work covers the range $1.4 \leq E_\gamma \leq 8.2$ MeV, and data from [6] $1.0 \leq E_\gamma \leq 7.6$ MeV. The photonuclear data from [50] are for $E_\gamma > 10.2$ MeV.

Finally, we note that our data show a natural continuation of the GDR tail towards lower γ energies. We stress again that the strength of the highest transition energies close to the neutron threshold is very likely to be strongly dependent on the initial and final state(s). Hence this is not quasicontinuum decay, but is still a real effect due to nuclear structure and spin selection rules. For another similar case, namely ^{89}Y(p, p') [39], there exist also inelastic photon scattering data [57], which display the same pattern as our data at high transition energies. This suppressed strength could be relevant also for e.g. (n, γ) cross-section calculations, if the neutron-capture reaction populates the same low initial spins. Thus one would expect a suppression of primary transitions to e.g. the ground state in the neutron-capture reaction as well.

According to the principle of detailed balance [58], one expects that the photoabsorption ("upward") strength equals the decay ("downward") strength. However, as discussed by Bartholomew *et al.* [53], the principle of detailed balance is only strictly fulfilled within the extreme statistical model. Hence, one would assume that this is only valid at high excitation energies where the NLD is high and the wave functions are strongly mixed. Moreover, the Brink hypothesis has been used [32] for calculating radiative widths at S_n, again assuming that the GDR tail extrapolated from photonuclear data to low γ energies could appropriately describe the decay process. Despite rather large uncertainties, it is fair to say that the present experimental data

from different reactions agree reasonably well and provide a quite consistent picture on the general shape of the γSF.

3.3. Comparison with theory

Although there are many phenomenological models and some more microscopic calculations available, they typically deviate considerably both in shape and magnitude. In Fig. 12 a selection of frequently used models are compared to the data. Note that we have used the global parameterization for the NLD models of [40] and [41] to test their predicitve power. For the NLD, none of the models reproduce the data over the full energy range. Clearly, only the microscopic approach is able to grasp some of the structures seen in the experimental results. Apparently, all the NLD models overshoot the data at high excitation energy. This could have severe consequences for e.g. calculations of reaction cross sections.

Also for the γSF models, the situation is rather confusing. Again, there is no model that can capture all features for the full γ-energy range. The smooth, phenomenological $E1$ models are quite appropriate close to the GDR, but are missing the upbend at low transitions energies. Even for the GLO model, which actually overshoots our ^{56}Fe data at $E_\gamma \approx 4-7$ MeV, underestimates the strength by a factor of ≈ 3 at $E_\gamma = 2.1$ MeV. This might not be a surprise, considering the possible $M1$ nature of the low-energy enhancement [19, 20], or an enhancement due to strong $E1$ continuum single-particle transitions [18], none of which are incorporated in the phenomenological models. Also, the microscopic models are undershooting the low-energy data as well–the ^{56}Fe data show a factor of ≈ 30 more strength than the quasi-particle random-phase approximation (QRPA) $E1$ strength [61]. However, the microscopic approaches do show structural features rather similar to the data between $7-10$ MeV. Clearly, the situation is at present far from satisfactory, and more theoretical work is required to understand in depth both NLDs and γSFs, preferably within the same theoretical framework.

4. Angular distributions, ^{57}Fe

In [16], it was shown that the low-energy upbend in ^{56}Fe is dominated by dipole transitions. Here, we apply the same type of analysis for the so-far unexplored ^{57}Fe upbend.

We use the various angles for which the NaI detectors are placed and extract angular distributions by sorting the data into (E_γ, E) matrices according to θ of the NaI detectors relative to the beam direction. As the $LaBr_3$ detectors were placed at only four angles, and had a rather high E_γ threshold, these were not used for this analysis. From the intensities as a function of angle, we can fit angular-distribution functions of the form [62, 63]

$$W(\theta) = A_0 + A_2 P_2(\cos\theta) + A_4 P_4(\cos\theta), \tag{12}$$

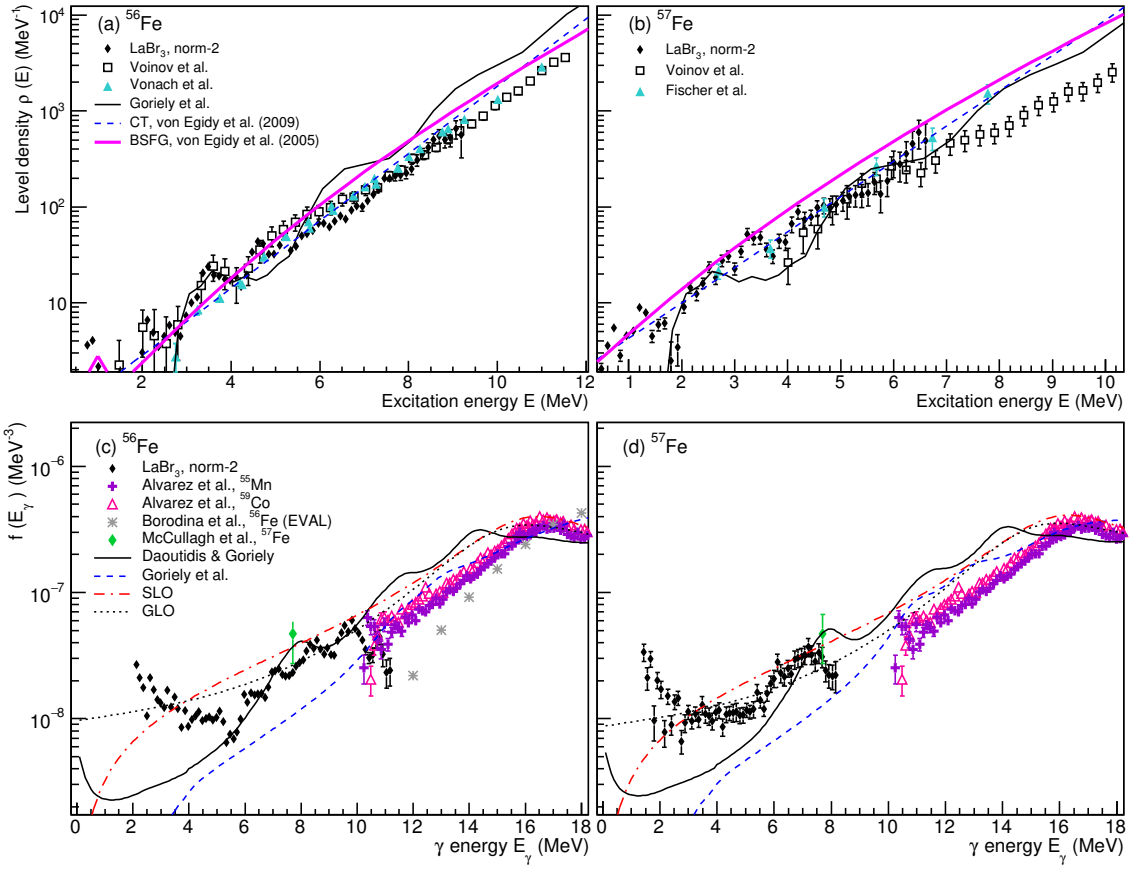

Figure 12. (Color online) Comparison of data and theoretical calculations for (a) ^{56}Fe NLD, (b) ^{57}Fe NLD, (c) ^{56}Fe γSF and (d) ^{57}Fe γSF. Microscopic level densities within the Hartree-Fock-Bogoliubov plus combinatorial approach are from [59]. Parameters for the CT model and the back-shifted Fermi-gas (BSFG) model are from [40] and [41], respectively. For the γSF models, GDR parameters for the standard Lorentzian (SLO) [32] and the Generalized Lorentzian (GLO) [45] are from [56]. The microscopic γSF calculations are from [60] (taken at $T = 1.4$ MeV) and [61].

where $P_k(\cos\theta)$ is a Legendre polynomial of degree k.

The normalized angular-distribution coefficients are given by $a_k = Q_k\alpha_k A_k/A_0$, where $Q_k \approx 1$ is the geometrical attenuation coefficient due to the finite size of the γ detectors, and α_k is the attenuation due to partial alignment of the nuclei relative to the beam direction. We estimate uncertainties in the intensities according to $\sigma_{\rm tot} = \sqrt{\sigma^2_{\rm stat} + \sigma^2_{\rm syst}}$. The statistical errors are given by $\sqrt{N}$ where N is the number of counts, and the systematic errors are deduced from the relative change in N for each symmetric pair of angles (37.4°,142.6°), (63.4°,116.6°), and (79.3°,100.7°). The statistical errors are typically $\approx 4\%$ or smaller, and the systematic errors are thus the dominant source of uncertainty. More details about the angular distributions are given in Appendix B.

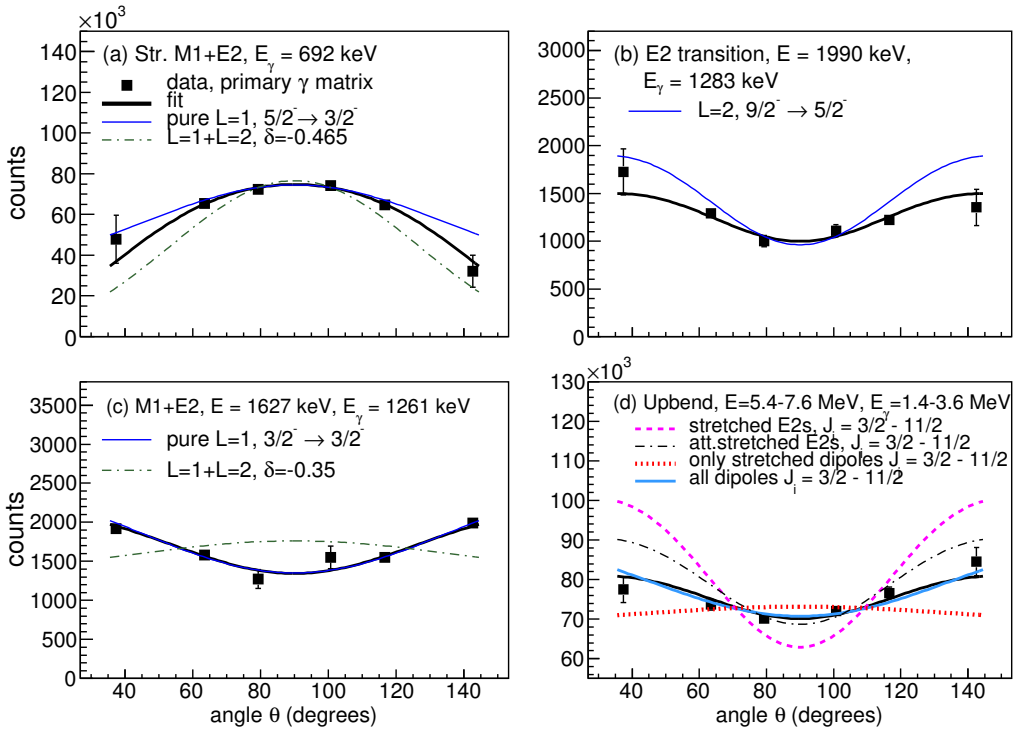
(a) Str. M1+E2, E_γ = 692 keV
data, primary γ matrix
fit
pure L=1, 5/2⁻→ 3/2⁻
L=1+L=2, δ=-0.465
counts
(b) E2 transition, E = 1990 keV,
E_γ = 1283 keV
L=2, 9/2⁻ → 5/2⁻
(c) M1+E2, E = 1627 keV, E_γ = 1261 keV
pure L=1, 3/2⁻ → 3/2⁻
L=1+L=2, δ=-0.35
counts
angle θ (degrees)
(d) Upbend, E=5.4-7.6 MeV, E_γ=1.4-3.6 MeV
stretched E2s, J_i = 3/2 - 11/2
att.stretched E2s, J_i = 3/2 - 11/2
only stretched dipoles J_i = 3/2 - 11/2
all dipoles J_i = 3/2 - 11/2
angle θ (degrees)

Figure 13. (Color online) Angular distributions for (a)–(c) single transitions and (d) the upbend region from primary transitions in ^{57}Fe.

Table 1. Angular-distribution coefficients of transitions measured in the present experiment. The theoretical $a_k^{\max}$ coefficients for complete alignment are taken from Ref. [63].

E (keV)	E_γ (keV)	$I_i \to I_f$	XL	δ	$a_2^{\max}$	a_2	$a_4^{\max}$	a_4
706	692	$5/2^- \to 3/2^-$	$M1+E2$	-0.465	-1.068	$-0.80(20)$	0.12	$-0.11(11)$
1627	1261	$3/2^- \to 3/2^-$	$M1+E2$	-0.35	-0.127	0.35(5)	0.00	$-0.05(14)$
1990	1283	$9/2^- \to 5/2^-$	$E2$	–	0.476	0.28(20)	-0.29	$-0.21(16)$

In figure 13 we show the angular distributions of known transitions in ^{57}Fe, and how they compare with the theoretical $a_k^{\max}$ values. All numbers are given in table 1. The comparison with the experimentally extracted a_2 coefficients and the theoretical maximum values for the known transitions shown in figure 13a,b, indicates an attenuation $\alpha_k \approx 0.6 - 0.75$.

The behavior of the $E_\gamma = 1261$ keV non-stretched‡ $M1+E2$ transition is somewhat puzzling, as [65] gives a rather large mixing parameter of -0.35 (see figure 13c). The shape of our data indicates a stronger contribution from the non-stretched $M1$ part, although we do have a large uncertainty in the a_4 parameter. Nevertheless, assuming a

‡ Transitions are called stretched for a maximum change in the angular momentum of the nuclear states, and non-stretched if the change is less than the maximum allowed for the given multipolarity.

pure $M1$ transition, one finds $a_2^{\max} = 0.400$, which is close to the experimental value of 0.35(5). We note that all a_4 parameters are consistent with 0 within their error bars.

For the upbend, we have fitted equation 12 to the primary spectra for the range $E = 5.4 - 7.6$ MeV and $E_\gamma = 1.4 - 3.6$ MeV with a_2 and a_4 as free parameters, obtaining $a_2 = 0.11(6)$ and $a_4 = -0.06(6)$ (see figure 13d). The uncertainty in a_4 is very large, but its value is small, indicating that contributions from stretched $E2$ transitions are not dominant. Moreover, we have made a fit of the data to the sum of Legendre polynomials for $J_i = 3/2 - 11/2$, with a weighting coefficient for the stretched and the non-stretched part. Here, we obtain 65(12) and 35(6)% for the non-stretched and the stretched transitions, respectively. Note that possible contributions from other spins and $E2$ transitions could modify these numbers, which should only be taken as a qualitative guidance.

However, when we fit only the sum of the stretched $E2$ Legendre polynomials for $J_i = 3/2 - 11/2$, we find a significantly worse agreement, see figure 13d. This is true also for the fit including the maximum experimental attenuation of ≈ 0.60, Fitting a sum of stretched and non-stretched dipoles and stretched $E2$ transitions yields a fit similar to that of only the attenuated $E2$s. Also a fit of only stretched dipole transitions is clearly not reproducing the data. The best fit (more than a factor of 5 better χ^2) is obtained with a sum of stretched and non-stretched dipole transitions, although small $E2$ contributions e.g. from $M1 + E2$ mixing cannot be ruled out.

To study the angular-distribution coefficients for the upbend in ^{57}Fe in more detail, we make individual fits of equation 12 to eight 300-keV wide excitation-energy cuts in the primary γ-ray matrix in the range $E = 5.4 - 7.6$ MeV, $E_\gamma = 1.4 - 3.6$ MeV. The resulting a_2 and a_4 coefficients are shown in figure 14. We obtain $\mathbf{a_2 = 0.10(2)}$ and $\mathbf{a_4 = -0.05(2)}$, in excellent agreement with the simultaneous fit to the whole region as shown in figure 13d.

The same trend was found in theoretical $\langle B(M1)\rangle$ values from shell-model calculations of ^{57}Fe [20], where non-stretched $M1$ transitions contributed most to the low-energy enhancement. Also, stretched $M1$ transitions dominated both experimentally [16] and theoretically [20] in the case of ^{56}Fe, bringing together a consistent picture, at least qualitatively. Hence, we conclude that the upbend structure in ^{57}Fe is also caused by dipole transitions, but for this case the non-stretched transitions seem to dominate.

5. Generalized Brink-Axel hypothesis: γSF as function of excitation energy

As the $LaBr_3$ detectors have excellent energy resolution and efficiency for high-energy γ rays, we make use of the technique described in [11, 21, 66] to extract the γSF as function of excitation energy.

We start with the primary γ-ray matrix $P(E_\gamma, E)$ obtained in section 2. We will now make the assumption that the NLD is the one determined in section 3, but the transmission coefficient $\mathcal{T}$ is now allowed to be dependent on both excitation energy

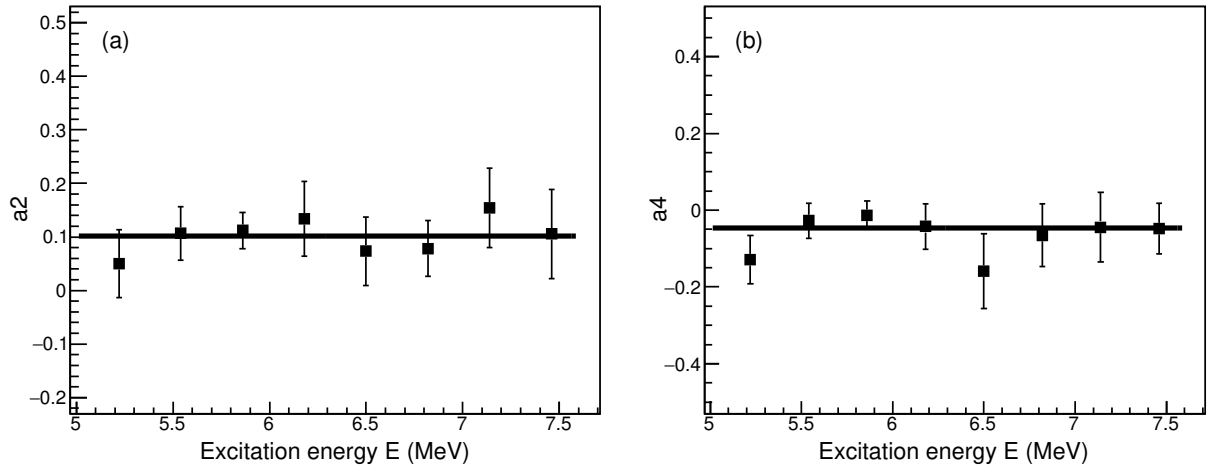

Figure 14. Extracted a_2 and a_4 coefficients from independent fits of 300-keV excitation-energy cuts in the ^{57}Fe primary matrices for the six CACTUS angles.

and γ-ray energy, $\mathcal{T}(E_\gamma, E)$. As $\rho(E_f)$ is known, we can in principle determine $\mathcal{T}(E_\gamma, E)$ for each excitation-energy bin just by dividing the primary γ matrix with the NLD: $\mathcal{T}(E_\gamma, E) \sim P(E_\gamma, E)/\rho(E_f)$, using our ansatz in equation 2. Specifically, we have

$$\rho(E - E_\gamma)\mathcal{T}(E_\gamma, E) = N(E)P(E_\gamma, E), \tag{13}$$

where $N(E)$ is a normalization factor in units MeV^{-1}, depending only on the initial excitation energy.

Now, this game can be played in two ways:

(a) We investigate $\mathcal{T}$ as function of *initial* excitation energy through the relation

$$\mathcal{T}(E_\gamma, E) = N(E)\frac{P(E_\gamma, E)}{\rho(E - E_\gamma)}. \tag{14}$$

We determine $N(E)$ by

$$N(E) = \frac{\int_0^E \mathcal{T}(E_\gamma)\rho(E - E_\gamma)\,\mathrm{d}E_\gamma}{\int_0^E P(E_\gamma, E)\,\mathrm{d}E_\gamma}. \tag{15}$$

Note that $\mathcal{T}(E_\gamma)$ is the normalized transmission coefficient from section 3. However, it will not influence the *shape* of the extracted $\mathcal{T}(E_\gamma, E)$ as it acts as a constant after integrating over all E_γ. Hence, it only serves to provide an approximate absolute normalization of $\mathcal{T}(E_\gamma, E)$.

(b) We can also find $\mathcal{T}$ as function of *final* excitation energy by

$$\mathcal{T}(E_\gamma, E_f) = N(E_\gamma + E_f)\frac{P(E_\gamma, E_f + E_\gamma)}{\rho(E_f)}, \tag{16}$$

where we keep in mind that $E_f + E_\gamma = E$. Again, we assume that $\mathcal{T}(E_\gamma)$ gives a good estimate of the absolute value and we can approximate the normalization for

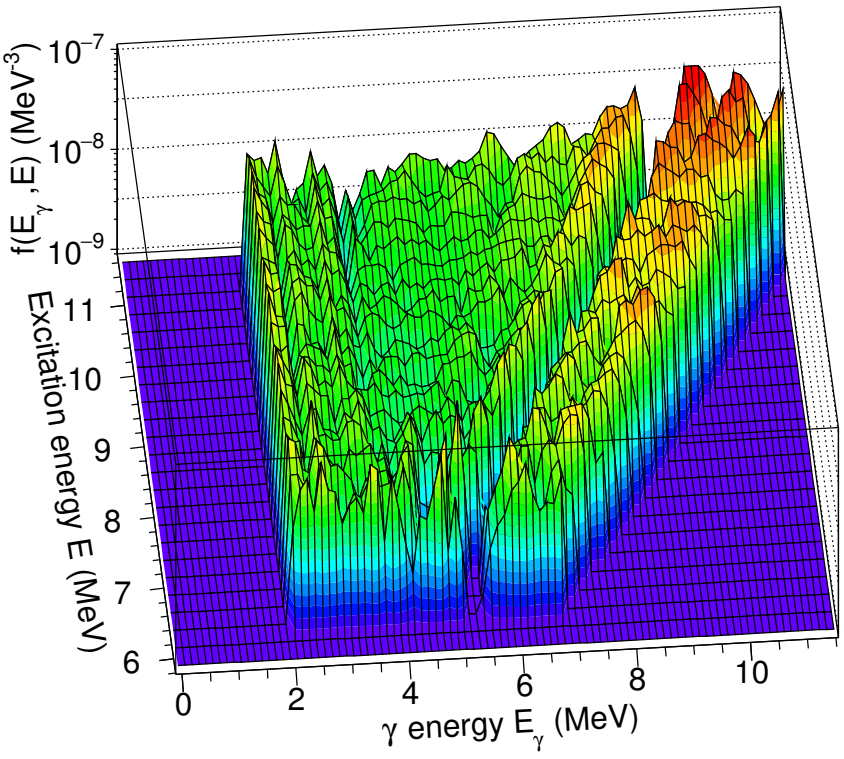

Figure 15. (Color online) Extracted γSFs as function of initial excitation energy for ^{56}Fe. Bins are 248 keV/channel for E and 124 keV/channel for E_γ.

a given final excitation energy E_f and for a specific E_γ fulfilling $E = E_f + E_\gamma$ by

$$N(E_\gamma + E_f) = \frac{\int_0^{E_f+E_\gamma} \mathcal{T}(E'_\gamma)\rho(E_f)\,\mathrm{d}E'_\gamma}{\int_0^{E_f+E_\gamma} P(E'_\gamma, E_f + E'_\gamma)\,\mathrm{d}E'_\gamma}. \quad (17)$$

The γSF as function of excitation energy is then easily calculated from the transmission coefficient by use of equation 10. The results are shown for ^{56,57}Fe in figures 15 and 16, respectively.

We observe that the decay strength to the ground state increases as function of both E and E_γ, which is fully consistent with the γSF determined previously in section 3 and the expected influence of the tail from the GDR. Moreover, we find that the γSF varies with initial excitation energy, but that the general shape is preserved: there is always an upbend at low E_γ and a rather flat distribution of strength in the middle E_γ region, before it again increases for high E_γ.

To investigate the fluctuations, following [66], we compare the average γSF for all initial excitation energies with the γSF obtained for a specific excitation-energy bin. We find that the fluctuations relative to the average γSF can be large, more than 100% for some γ-ray energies and E. Also, the fluctuations are in some cases significantly larger than the error bars. Therefore, it seems that although the overall shape of the

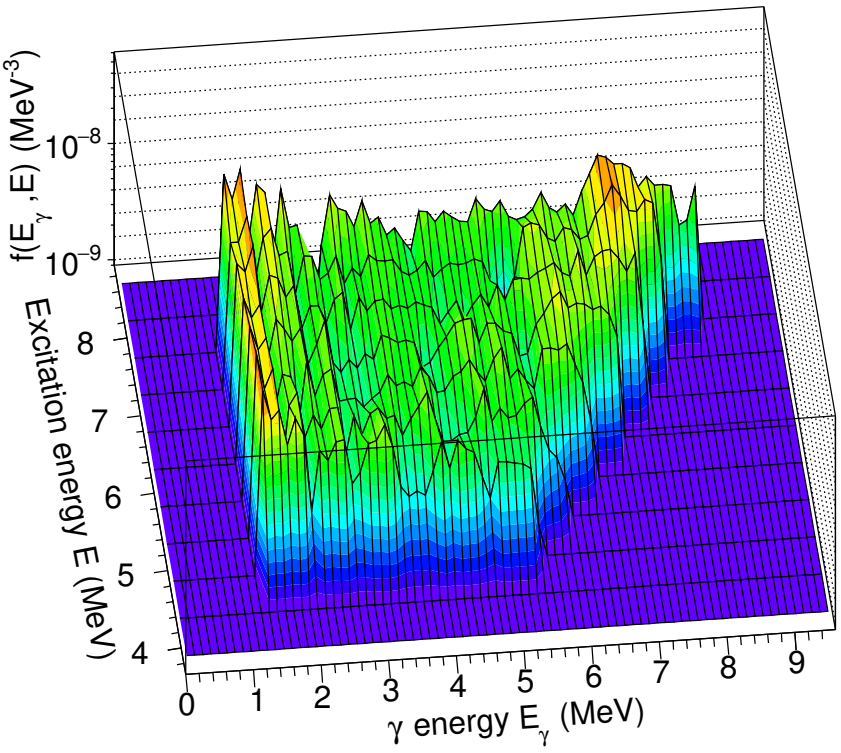

Figure 16. (Color online) Extracted γSFs as function of initial excitation energy for ^{57}Fe. Bins are 480 keV/channel for E and 120 keV/channel for E_γ.

γSF is indeed preserved in agreement with the generalized Brink-Axel hypothesis, the γSF for a specific transition energy and excitation energy could have a large deviation, in particular when the excitation-energy bin is narrow and containing rather few levels.

Finally, we also investigate the γSF for a specific final excitation energy. We have chosen the ground state in ^{56}Fe and the ground-state band ($1/2^-$, $3/2^-$, $5/2^-$) in ^{57}Fe. The γSF for this E_f is then compared to a typical γSF at a high initial E, see figures 17 and 18. Again, we observe that the general trend is preserved, although significant deviations are present, for example for the ^{56}Fe strength at $E_\gamma \approx 9.7$ MeV. This is interpreted to be caused by Porter-Thomas fluctuations, which are expected to be large when the final and/or the initial NLD is low [21].

6. Summary and outlook

We have presented data on ^{56,57}Fe from $(p, p'\gamma)$ reactions using NaI and $LaBr_3$ crystals simultaneously. We confirm the upbend in these isotopes, which represents an increase in strength of a factor $\approx 3 - 30$ relative to commonly used models for the $E1$ strength

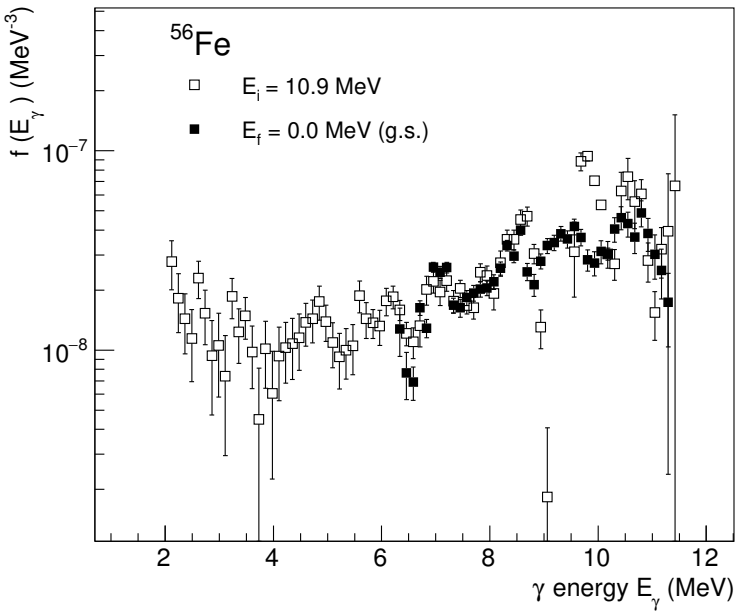

Figure 17. Extracted γSF for the ^{56}Fe ground state as E_f (black points) and for $E = 10.9$ MeV.

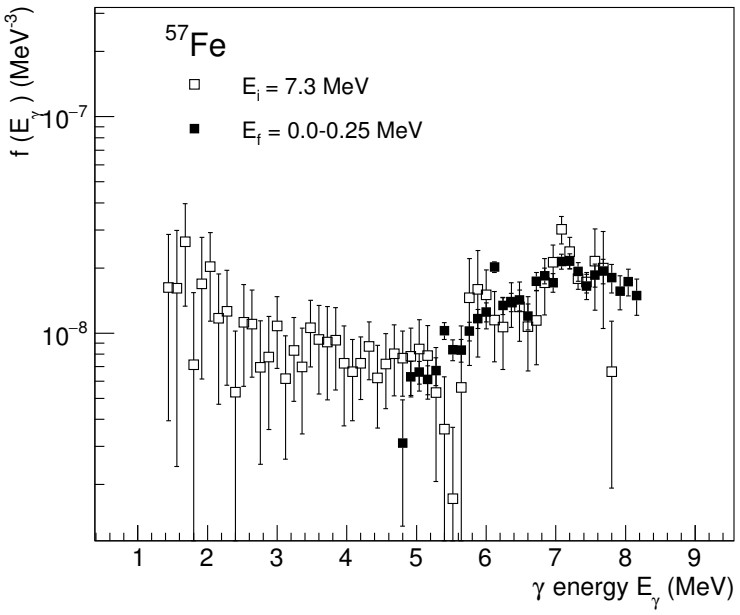

Figure 18. Extracted γSF for the ^{57}Fe ground-state band, $E_f = 0.0 - 0.25$ MeV (black points) and for $E_i = 7.3$ MeV.

at low transition energies. Moreover, external data involving heavier projectiles and/or

ejectiles are typically within the error bars. The lower NLD in ^{56}Fe for $E \approx 5 - 7.5$ MeV compared to the external data is attributed to the lower spins reached in the (p, p') reaction.

We have shown angular distributions of the upbend for ^{57}Fe for the first time. Our results indicate a mix of stretched and non-stretched dipoles contributing to the upbend, in agreement with recent shell-model calculations. Moreover, we have investigated the excitation-energy dependence of the γSF. The data show that the general trends are preserved in accordance with the Brink-Axel hypothesis. However, we also encounter large fluctuations, which seem to be due to strong Porter-Thomas fluctuations caused by the low level density in these light nuclei.

Currently, the CACTUS array is in the process of being replaced by OSCAR (Oslo SCintillator ARray), for which all the NaI detectors are replaced with 3.5 *in.* × 8 *in.* $LaBr_3$(Ce) detectors, and a new frame and target chamber are being built as well. This new array will open up a wealth of new opportunities, such as discriminating against neutrons above S_n to extract the γSF at even higher energies, gating on discrete transitions to study the feeding pattern and thus spin dependencies of the NLD and γSF, and many more. We expect to be able to study the upbend and Porter-Thomas fluctuations in much more detail with this new equipment.

Comparing our data with frequently used NLD and γSF models clearly shows the need for better theoretical predictions. After all, here we present data on stable nuclei; the predictive power for unstable, highly exotic nuclei involved in e.g. the nucleosynthesis is definitely unsatisfactory. To improve the situation, more data on both stable and unstable nuclei are required to help testing and constraining available calculations, as well spurring new theoretical approaches and methods in nuclear physics.

Acknowledgments

The authors wish to thank J.C. Müller, E.A. Olsen, A. Semchenkov and J. C. Wikne at the Oslo Cyclotron Laboratory for providing excellent experimental conditions. This work was financed by the Research Council of Norway (NFR), project grant no. 205528, and through ERC-STG-2014 under grant ggreement no. 637686. S. S. and G. M. T. acknowledge financial support by the NFR under project grant no. 210007 and 222287, respectively. A. V. V. acknowledges funding from the Department of Energy, grant no. DE-NA0002905. M. W. acknowledges support by the National Research Foundation of South Africa under grant no. 92789.

References

[1] Arnould M and Goriely S 2003 *Phys. Rep.* **384** 1
[2] Arnould M, Goriely S, and Takahashi K 2007 *Phys. Rep.* **450** 97
[3] Aliberti G, Palmiotti G, Salvatores M, and Stenberg C G 2004 *Nucl. Sci. Eng.* **146** 13
[4] Aliberti G *et al.* 2006 *Ann. Nucl. Energy* **33** 13

[5] Schiller A, Bergholt L, Guttormsen M, Melby E, Rekstad J, and Siem S 2000 *Nucl. Instrum. Methods Phys. Res. A* **447** 498
[6] Voinov A *et al.* 2004 *Phys. Rev. Lett.* **93** 142504
[7] Larsen A C *et al.* 2007 *Phys. Rev. C* **76** 044303
[8] Bürger A *et al.* 2012 *Phys. Rev. C* **85** 064328
[9] Voinov A V *et al.* 2010 *Phys. Rev. C* **81** 024319
[10] Renstrøm T *et al.* 2016 *Phys. Rev. C* **93** 064302
[11] Guttormsen M *et al.* 2005 *Phys. Rev. C* **71** 044307
[12] Wiedeking M *et al.* 2012 *Phys. Rev. Lett.* **108** 162503
[13] Tveten G M *et al.* 2016 *Phys. Rev. C* **94** 025804
[14] Kheswa B V *et al.* 2015 *Phys. Lett. B* **744** 268
[15] Simon A *et al.* 2016 *Phys. Rev. C* **93** 034303
[16] Larsen A C *et al.* 2013 *Phys. Rev. Lett.* **111** 242504
[17] Larsen A C and Goriely S 2010 *Phys. Rev. C* **82** 014318
[18] Litvinova E and Belov N 2013 *Phys. Rev. C* **88** 031302(R)
[19] Schwengner R, Frauendorf S, and Larsen A C 2013 *Phys. Rev. Lett.* **111** 232504
[20] Brown B A and Larsen A C 2014 *Phys. Rev. Lett.* **113** 252502
[21] Guttormsen M *et al.* 2016 *Phys. Rev. Lett.* **116** 012502
[22] Guttormsen M, Bürger A, Hansen T E, and Lietaer N 2011 *Nucl. Instrum. Methods Phys. Res. A* **648** 168
[23] Guttormsen M *et al.* 1990 *Phys. Scr. T* **32**54
[24] Nicolini R *et al.* 2007 *Nucl. Instrum. Methods Phys. Res. A* **582** 554
[25] Giaz A *et al* 2013 *Nucl. Instrum. Methods Phys. Res. A* **729** 910
[26] Wiedeking M *et al* 2016 *Phys. Rev. C* **93** 024303
[27] Guttormsen M *et al.* 1996 *Nucl. Instrum. Methods Phys. Res. A* **374** 371
[28] Crespo Campo L *et al.* 2016 *Phys. Rev. C* (in press)
[29] Guttormsen M, Ramsøy T, and Rekstad J 1987 *Nucl. Instrum. Methods Phys. Res. A 255* 518
[30] Dirac P A M 1927 *Proc. R. Soc. London A* **114** 243
[31] Fermi E 1950 *Nuclear Physics* (University of Chicago Press, Chicago)
[32] Brink D M 1955 *Dr. Phil. thesis, Oxford University*
[33] Axel P 1962 *Phys. Rev.* **126** 671
[34] Bohr A and Mottelson B 1969 *Nuclear Structure* (Benjamin, New York, Vol. I)
[35] Larsen A C *et al.* 2011 *Phys. Rev. C* **83** 034315
[36] Porter C E and Thomas R G 1956 *Phys. Rev.* **104** 483
[37] Data from the NNDC On-Line Data Service database as of August 2016; available at `http://www.nndc.bnl.gov/nudat2/`
[38] Capote R *et al.* 2009 *Nucl. Data Sheets* **110** 3107; *Reference Input Parameter Library (RIPL-3)*, available at `http://www-nds.iaea.org/RIPL-3/`
[39] Larsen A C *et al.* 2016 *Phys. Rev. C* **93** 045810
[40] von Egidy T and Bucurescu D 2009 *Phys. Rev. C* **80** 054310
[41] von Egidy T and Bucurescu D 2005 *Phys. Rev. C* **72** 044311; 2006 *Phys. Rev. C* **73** 049901(E)
[42] Ericson T 1959 *Nucl. Phys.* **11** 481
[43] Ericson T 1960 *Adv. Phys.* **9** 425
[44] Voinov A, Guttormsen M, Melby E, Rekstad J, Schiller A, and Siem S 2001 *Phys. Rev. C* **63** 044313
[45] Kopecky J and Uhl M 1990 *Phys. Rev. C* **41** 1941
[46] Voinov A *et al.* 2006 *Phys. Rev. C* **74** 014314
[47] Vonach H K *et al.* 1966 *Phys. Rev.* **149** 844
[48] Voinov A *et al.* 2007 *Phys. Rev. C* **76** 044602
[49] Fischer F F *et al.* 1984 *Phys. Rev. C* **30** 72
[50] Alvarez R A, Berman B L, Faul D D, Lewis Jr F H, and Meyer P 1979 *Phys. Rev. C* **20** 128

[51] Borodina S S, Varlamov A V, Varlamov V V, Ishkhanov B S, and Mokeev V I 2000 *Moscow State Univ. Inst. of Nucl. Phys. Reports No. 2000* 6/610
[52] Dietrich S S and Berman B L 1988 *At. Data. and Nucl. Data Tables* **38**, 199 and references therein
[53] Bartholomew G A, Earle E D, Ferguson A J, Knowles J W, and Lone M A 1973 *Adv. Nucl. Phys.* **7** 229
[54] Jackson H E and Strait E N 1971 *Phys. Rev. C* **4** 1314
[55] McCullagh C M, Stelts M L, and Chrien R E 1981 *Phys. Rev. C* **23** 1394
[56] Belgya T *et al.* 2006 *Handbook for calculations of nuclear reaction data, RIPL-2* **IAEA-TECDOC-1506**, available at `http://www-nds.iaea.org/RIPL-2/`
[57] Benouaret N, Schwengner R, Rusev G, Dönau F, Beyer R, Erhard M, Grosse E, Junghans A R, Kosev K, Nair C, Schilling K D, Wagner A, and Bendjaballah N 2009 *Phys. Rev. C* **79** 014303
[58] Blatt J M and Weisskopf V F 1952 *Theoretical Nuclear Physics*, John Wiley & Sons, Inc., New York
[59] Goriely S, Hilaire S, and Koning A J 2008 *Phys. Rev. C* **78** 064307
[60] Daoutidis I and Goriely S 2012 *Phys. Rev. C* **86** 034328
[61] Goriely S, Khan E and Samyn M 2004 *Nucl. Phys.* **A739** 331
[62] Litherland A E and Ferguson A J 1961 *Can. J. Phys.* **39** 788
[63] der Mateosian E and Sunyar A W 1974 *At. Data and Nucl. Data Tables* **13** 391
[64] Krane K S 1978 *At. Data and Nucl. Data Tables* **22** 269
[65] Data from the Evaluated Nuclear Structure Data File (ENSDF) as of August 2016, available at `http://www.nndc.bnl.gov/ensdf/`
[66] Guttormsen M *et al.* 2011 *Phys. Rev. C* **83** 014312

Appendix A. Data tables for normalizations

Table A1. Neutron resonance parameters D_0 and $\langle\Gamma_{\gamma 0}\rangle$ from [38], and spin cutoff parameters from global systematics of [40]; A_f is the final nucleus following neutron capture, J_t is the ground-state spin of the target nucleus, S_n is the neutron-separation energy, D_0 is the s-wave level spacing [38], σ is the spin-cutoff parameter from equation (6), Pa' is the deuteron shift as defined in [40], and $\rho(S_n)$ is the total level density calculated from equation 5. Finally, $\rho^{\rm syst}$ is the total level density at S_n as predicted from the global systematics of [40]. †Estimated from systematics.

A_f	J_t	S_n (MeV)	D_0 (keV)	$\sigma(S_n)$	Pa' (MeV)	$\rho(S_n)$ (10^3 MeV^{-1})	$\rho^{\rm syst}(S_n)$ (10^3 MeV^{-1})	$\langle\Gamma_{\gamma 0}\rangle$ (meV)
^{55}Fe	0	9.298	20.5(14)	3.41	0.463	1.19(9)	1.28	1600(700)
^{56}Fe	3/2	11.197	3.36(124)†	3.47	2.905	2.18(59)†	2.94	1900(600)†
^{57}Fe	0	9.298	25.4(22)	3.35	0.211	0.926(80)	1.14	920(410)
^{58}Fe	1/2	10.044	7.05(70)	3.44	2.874	1.81(18)	3.49	1850(500)
^{59}Fe	0	6.581	21.6(26)	3.30	0.470	1.06(13)	1.01	1130(110)

Table A2. Neutron resonance parameters D_0 from [38], and spin cutoff parameters from global systematics of [41]; A_f is the final nucleus following neutron capture, J_t is the ground-state spin of the target nucleus, S_n is the neutron-separation energy, σ is the spin-cutoff parameter from equation (7), D_0 is the s-wave level spacing [38], a and E_1 are the level density parameter and energy shift from [41], and $\rho(S_n)$ is the total level density calculated from equation 5. Finally, $\rho^{\rm syst}$ is the total level density at S_n as predicted from the global systematics of [41]. †Estimated from systematics.

A_f	J_t	S_n (MeV)	D_0 (keV)	$\sigma(S_n)$	a (1/MeV)	E_1 (MeV)	$\rho(S_n)$ (10^3 MeV^{-1})	$\rho^{\rm syst}(S_n)$ (10^3 MeV^{-1})
^{55}Fe	0	9.298	20.5(14)	4.02	5.817	-0.524	1.62(11)	2.00
^{56}Fe	3/2	11.197	$3.30^{+0.9}_{-0.6}$†	4.05	6.196	0.942	2.87(68)†	4.22
^{57}Fe	0	9.298	25.4(22)	3.83	6.581	-0.523	1.20(10)	1.62
^{58}Fe	1/2	10.044	7.05(70)	3.93	6.936	0.942	2.32(23)	4.66
^{59}Fe	0	6.581	21.6(26)	3.70	7.297	-0.424	1.32(16)	1.38

Table A3. Parameters for the constant-temperature interpolation for the different normalization options. Both parameters T and E_0 are given in MeV.

	Norm-1						Norm-2					
Nucleus	Lower		Middle		Upper		Lower		Middle		Upper	
	T	E_0	T	E_0	T	E_0	T	E_0	T	E_0	T	E_0
^{56}Fe	1.41	0.320	1.40	−0.034	1.38	−0.169	1.40	−0.070	1.35	0.045	1.30	0.232
^{57}Fe	1.32	−1.618	1.30	−1.575	1.29	−1.601	1.31	−1.882	1.29	−1.829	1.28	−1.848

Appendix B. More details for the angular distributions

For the Legendre polynomials we have

$$P_2(\cos\theta) = \frac{1}{2}\left[3(\cos\theta)^2 - 1\right], \tag{B.1}$$

$$P_4(\cos\theta) = \frac{1}{8}\left[35(\cos\theta)^4 - 30(\cos\theta)^2 + 3\right]. \tag{B.2}$$

In the case of a fully aligned state with respect to the beam direction ($\alpha_k = 1$), the $a_k^{\rm max}$ coefficients are given by [63]

$$a_k^{\rm max}(J_i L L' J_f) = \frac{B_k}{1+\delta^2}\left[F_k(J_f L L J_i) + 2\delta F_k(J_f L L' J_i) + \delta^2 F_k(J_f L' L' J_i)\right]. \tag{B.3}$$

Here, J_i, J_f are the spins of the initial and final level, L, L' are transition multipolarities, δ is the mixing ratio between the multipolarities defined according to [64]:

$$\delta = \frac{\langle J_f || E(L+1) || J_i\rangle}{\langle J_f || M(L) || J_i\rangle}. \tag{B.4}$$

Here, $E(L+1)$ is the electric transition operator for multipolarity $L+1$, and $M(L)$ is the magnetic transition operator for multipolarity L. Further, the B_k, F_k coefficients are defined in [63], where also values for the product $B_k F_k$ are tabulated.

We investigate known transitions in ^{57}Fe, such as the 692-keV γ ray decaying from the level at 706 keV, where $J_i = 5/2^-$ and $J_f = 3/2^-$, and the transition is known to be of $M1 + E2$ type with a mixing ratio $\delta = -0.465$ [65]. We get

$$a_2^{\max} = \frac{1}{1+0.465^2}[B_2F_2(3/2,1,1,5/2) + 2\cdot(-0.465)\cdot B_2F_2(3/2,1,2,5/2) + 0.465^2 B_2F_2(3/2,2,2,5/2)].$$

From [63] we have $B_2F_2(3/2,1,1,5/2) = -0.400$, $B_2F_2(3/2,1,2,5/2) = 1.014$, and $B_2F_2(3/2,2,2,5/2) = 0.204$, giving $a_2^{\max} = -1.068$. For $a_4^{\max}$, we find

$$a_4^{\max} = \frac{1}{1+0.465^2}[0.465^2 B_4F_4(3/2,2,2,5/2)];$$

with $B_4F_4(3/2,2,2,5/2) = 0.653$, we get $a_4^{\max} = 0.116$. Similarly, we get for an $E2$ transition with $J_i = 9/2, J_f = 5/2$ and no mixing ($\delta = 0$), $a_2^{\max} = 0.476$ and $a_4^{\max} = -0.286$.